Proton computed tomography of human specimens

K M Hanson, J N Bradbury, R A Koeppe, R J Macek, D R Machen,
R Morgado, M A Paciotti, S A Sandford and V W Steward†

Los Alamos National Laboratory, Los Alamos, NM 87545, USA
† University of Chicago, Chicago, Illinois, USA

Abstract. The experimental procedure and results of a comparative study of the imaging characteristics of proton and x-ray CT scans are presented. Scans of a human brain and heart are discussed. The proton produced images are found to be similar in information content while providing a decided dose advantage.

1. Introduction

In previous work (Hanson *et al* 1981) we demonstrated experimentally the dose advantage in computed tomography (CT) afforded by the proton energy-loss method compared to the standard x-ray absorption technique. With this dose advantage, it is feasible to achieve CT reconstructions with significantly better density sensitivity at a given dose by using protons instead of x-rays. Since in proton CT it is the relative linear stopping power that is imaged instead of the linear attenuation coefficient as in x-ray CT, it might be expected that the two modalities would produce entirely different images of human anatomy. In this paper we present the experimental procedure and some of the results of a study to compare the imaging characteristics of proton and x-ray CT scans of human organs. A comprehensive comparison of the specimen scans will be presented elsewhere.

The apparatus is described in section 2 and the experimental method is explained in section 3. The results of the experiment and the comparison with x-ray CT scans are presented in section 4. Concluding remarks are made in section 5.

2. Apparatus

The P^3-West channel at the Clinton P Anderson Meson Physics Facility (LAMPF) produced protons of excellent energy stability and with a small spot size. Figure 1 shows the experimental layout. The proton beam was scanned across the phantom by a bending magnet positioned 5.2 m upstream from the water bath. A vacuum box extended the channel vacuum up to a window just in front of the water bath to prevent multiple scattering degradation of the high quality beam spot. The beam possessed a waist near the entrance of the water bath with a horizontal width of about 1 mm FWHM and a divergence of 6 milliradians (FWHM). The vertical height of the beam was limited by a slit to 1.0 cm. The beam energies in the experiment, 224 to 236 MeV, were restricted to a 0.4% FWHM energy spread.

The proton beam was swept horizontally back and forth across the phantom by exciting the scan magnet with a triangular current waveform. The current did not
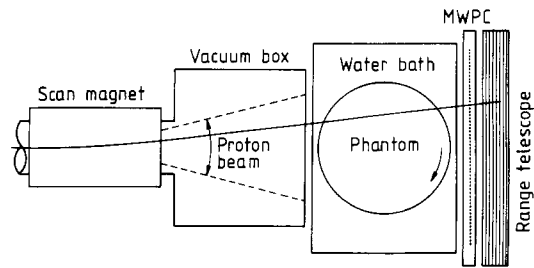
Figure 1. Schematic layout of apparatus.

change polarity so the undeflected beam passed near one edge of the water bath. The water bath thickness was 26.6 cm including the 0.32 cm thick aluminum entrance and exit walls and was constant over its face to within 0.02 cm. The water bath was used in this experiment to limit the dynamic range required of the range detector. Phantom rotation was accomplished by a servomechanism that was controlled by the on-line PDP-11 computer.

Two multiwire proportional chambers positioned 5 cm past the water bath were used to detect the horizontal and vertical position of each exit proton. With 2 mm wire spacing, these chambers employed an amplifier on each wire and operated with a gas mixture of 75% argon, 1% freon (13B-1), 24% isobutane, and 0.4% 1-propanol. No loss of efficiency was observed at the proton flux densities encountered in this experiment (less than 4000 $mm^{-2} s^{-1}$). Both chambers were required in the event trigger. Nine active wires were used in the vertical plane to limit the height of the multiply scattered beam accepted by the system. This restriction, together with the 1.0 cm high entrance collimator, produced a nearly uniform beam profile, 1 cm high, throughout the water bath. Twenty-nine percent of the protons emerging from the water bath fell outside of this nine-wire region and were thus lost to this experiment. A more complete detector system could make use of all of the existing protons by incorporating the protons with extreme scattering in adjacent slices.

A range telescope recorded the residual range of each proton. Each of the 32 counters in the stack was 5.1 cm by 38.1 cm NE102 scintillator machined to a thickness of 3.18 mm with a tolerance of 0.05 mm. The first two counters were used in the event trigger and did not contribute to the dynamic range of the detector.

The event data were processed by fast data encoders for the wire chamber and range telescope, a CAMAC auxiliary controller system and a PDP-11/45. The data encoder, designed and built at Los Alamos (Brown 1979), was located 6.5 m from the proportional chambers. It employed priority encoding logic to determine the highest wire to fire. Non-adjacent multiple-hit events were rejected by the encoder logic. The deadtime for latching and encoding an event was 130 ns, provided successive events were not on the same wire. An additional 50 ns deadtime was incurred for a repeated hit on the same wire, an occurrence with a maximum probability 12%. The range telescope data were latched by a Lecroy 2341A coincidence register and then priority-encoded to determine the last counter in the telescope to fire. The 2341A LRS output circuit was modified to allow direct access to the data by the priority encoder. The encoded chamber and range counter positions for each event were combined into one 16-bit word and loaded into a fast first-in, first-out memory. This 16-word-deep memory buffered the randomly occurring events from the read-out system that could only accept an event from the output of the memory every 2 μs. This buffering significantly reduced the effective deadtime of the data acquisition circuitry.

The LAMPF Auxiliary Crate Controller (ACC) (Machen 1979, 1980), residing in a standard CAMAC crate, was central to the data acquisition. During the beam macropulse, the ACC read event data from the buffer memory, also located in the CAMAC crate, and stored the data in its own 256-word memory at a 0.5 MHz rate. Between macropulses, the ACC analysed the data as described in the next section. The ACC contained two processors, a DEC LSI-11/2 microcomputer, and an AM 2900-based, bit-sliced microprocessor. The LSI-11 had overall control of the data acquisition. Its Q-bus, expanded to include new functions, was common to all other ACC elements. The bit-sliced processor, running at a 140 ns cycle time, performed the bulk of the data acquisition and analysis. A control port allowed access to the CAMAC dataway by either processor. The CAMAC short cycle (300 ns) mode was used for maximum speed. The online PDP-11/45 had direct access to the Q-bus and its associated memories over the CAMAC branch highway and through an access port module. The PDP-11/45 read the analysed results for each macropulse and wrote them on magnetic tape for subsequent analysis. Also written on tape were the phantom rotation angle and readings of a Hall probe placed inside the scan magnet.

3. Experimental procedure

The CT scanning procedure was performed by taking the complete, almost parallel, projection data at each position of the phantom followed by a 1° rotation of the phantom to the next viewing angle. Typically two to four sweeps of the proton beam were made at each viewing angle. Each 30 cm sweep of the proton beam took 5 s. As the beam swept across the phantom, data were taken every 8.3 ms. Typically, 255 events were collected during each 650 µs macropulse. With a 14% deadtime arising from the inefficiency in reversal of the beam direction, 60×10^6 events could be collected and processed in a one-hour period. At these rates, 29% of the potentially good events were lost because of the combined deadtime of the proportional chambers and all subsequent electronics.

The events collected in each beam macropulse were analysed by the ACC processor in the 7.7 ms period before the next macropulse. A histogram of the events was produced as a function of proton exit position. The mean exit position was determined by an iterative, weighted moment calculation (Hanson *et al* 1981). Uniform weighting was employed in the first iteration. The second iteration used a rectangular weighting function, 23 wires wide, centred on the mean position found in the first iteration. The resulting first moment was taken as the mean proton position. Next the events were sorted into a two-dimensional histogram corresponding to nine MWPC wire positions centred on the mean exit position and to the 32 range telescope bins. The mean range was determined for each range histogram using the same algorithms as described above. The rectangular weighting function used in the second iteration was 7.0 counters wide and was centred 1.7 counters deeper than the first mean in order to compensate for the long plateau before the peak (figure 2). This on-line analysis procedure not only eliminated the need for later analysis but also reduced the number of computer words needed to be transmitted and recorded from 255 to 31. Consequently, the results from 60×10^6 events could easily be stored on two 2400 ft magnetic tapes.

One disadvantage of the on-line analysis was the loss of the original data. During the early scans, the offset used in the mean range calculation was improperly set set at 0.2 counters. This 1.5 counter error led to a 37% loss in range accuracy that could not be regained since the original data were not available. For the purpose of the dose
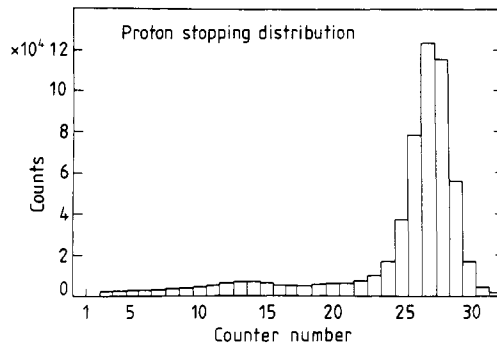
Figure 2. The proton stopping distribution measured by the range telescope for 10^6 events. Each counter has a width equivalent to 0.335 g cm^{-2} of water.

calculation, the number of events used for these early runs will be given henceforth in terms of the number of event that would be required with the proper offset to match the fitting accuracy achieved. Thus 110×10^6 events taken in the early runs are equivalent in accuracy to 43×10^6 events recorded in the later runs.

The range telescope was calibrated by scanning the water bath with a variable number of flat aluminum plates placed in front of it. A typical range counter response is shown in figure 3. The shape of the response was similar at all of the mean ranges
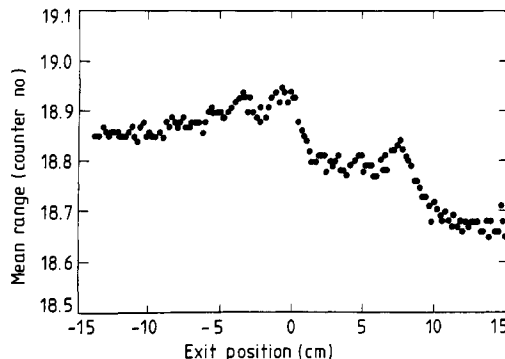

Figure 3. Typical range counter response obtained by scanning water bath and flat aluminum plate.

studied from 6.6 to 24.8 counters. The change from one plate to the next led to an overall calibration of 0.335 g cm^{-2} equivalent water thickness per counter. For the ratio of linear stopping of aluminum to that of water at 230 MeV (Janni 1966), 2.11 was used. This calibration checks well with the value obtained from the actual thickness of the counters plus intervening aluminum foil, 0.332 g cm^{-2}. The variation in range counter response with exit position shown in figure 3 was taken into account in the reconstruction process as described below. The observed 87 mg cm^{-2} peak-to-peak variation is caused by variations in water bath thickness, variation of depth with proton angle and non-uniformities in the range telescope.

A series of 112 stability runs were taken in which 30×10^6 events were acquired over a 30 min period. These data were analysed by the on-line processor. A typical run contained 1033 macropulses or 167,000 events in the range peaks. The RMS deviation

of the mean range calculated in the runs was observed to be 0.0046 ± 0.0003 counters or 1.54 ± 0.10 mg cm^{-2}. The expected RMS deviation was 1.21 mg cm^{-2} taking into account the effect on the fitting statistics arising from the use of the rectangular weighting function (Hanson *et al* 1981). Thus, the range measurements were stable to better than 1 mg cm^{-2} with 90% confidence.

In preparation for reconstruction the data were sorted into 360 parallel projections at 0.5° intervals in position bins 1.0 mm in width. Exit position information was used to make small alterations to the straight-through trajectories as described by Hanson *et al* 1981. This, as well as the 3° fan angle, provided measurements at angles other than just the phantom rotation angles. The Hall probe readings were used to determine the entrance positions. The data from each phantom angle were normalised using the water bath scan segments on each side of the phantom. A standard filtered back-projection algorithm was used to obtain 256×256 reconstructions 28 cm in diameter. The ramp filter was multiplied by a Gaussian function with half height occurring at 2.3 cm^{-1}. The sorting took about 1 min and the reconstruction about 2 min on a CDC 7600 computer.

The first reconstructions showed many circular artifacts arising from the fluctuations in the range telescope calibration (figure 3). This calibration was incorporated by producing a reconstruction from the water bath scan data. This reconstruction was smoothed over roughly four pixels to reduce the effect of noise fluctuations and then subtracted from the phantom reconstructions. The circular artifacts were almost completely eliminated by this procedure.

The human specimens came from autopsies performed at the New Mexico Medical Examiner's office. The specimens were suspended inside plastic cannisters in a gelatin mixture. The cannisters were packed in ice to avoid tissue deterioration until all CT scans were completed as most of the specimens were not fixed in formalin. Every attempt was made to scan the specimens as soon after death as possible since it is known that the x-ray attenuation coefficients of tissue samples change rapidly after death (Wittenberg *et al* 1977). Formalin fixation was avoided because its effect upon proton stopping power compared to that upon x-ray attention coefficients is unknown.

4. Results

In this section we will compare the proton reconstructions with those obtained on two commercial x-ray CT scanners, the GE CT/T 8800 at the Presbyterian Medical Centre and the Technicare Δ2020 at Lovelace Clinic in Albuquerque. The Δ2020 was not equipped with the recently introduced 'shaped filter' while the GE 8800 had its standard compensation wedge. The 34 cm scan diameter was used on the GE 8800 in the half-scan mode (456 mA s) for all but the five-pin phantom which used the full scan mode (768 mA s). The scanner operated at 120 kV$_p$. The Δ2020 was operated at 120 kV$_p$, 200 mA s at both 25 cm and 40 cm scan diameters. In order to allow side-by-side comparison of the scans, the reconstructions from the commercial scanners were taken from the archival tapes and displayed on the same unit as the proton scans, a Comtal 8000. To accomplish this, the 512×512 Comtal display matrix was filled by a 28 cm × 28 cm section of the reconstructions by bilinear interpolation. The proton scans were displayed in the same way. In all cases, the images were displayed so that an 18% range of reconstruction values relative to water completely filled the available gray scale.

Figure 4 shows the scans obtained of a phantom used to determine slice thickness. The phantom contained three ramp blocks. The ramps were made by milling a 2.0-mm
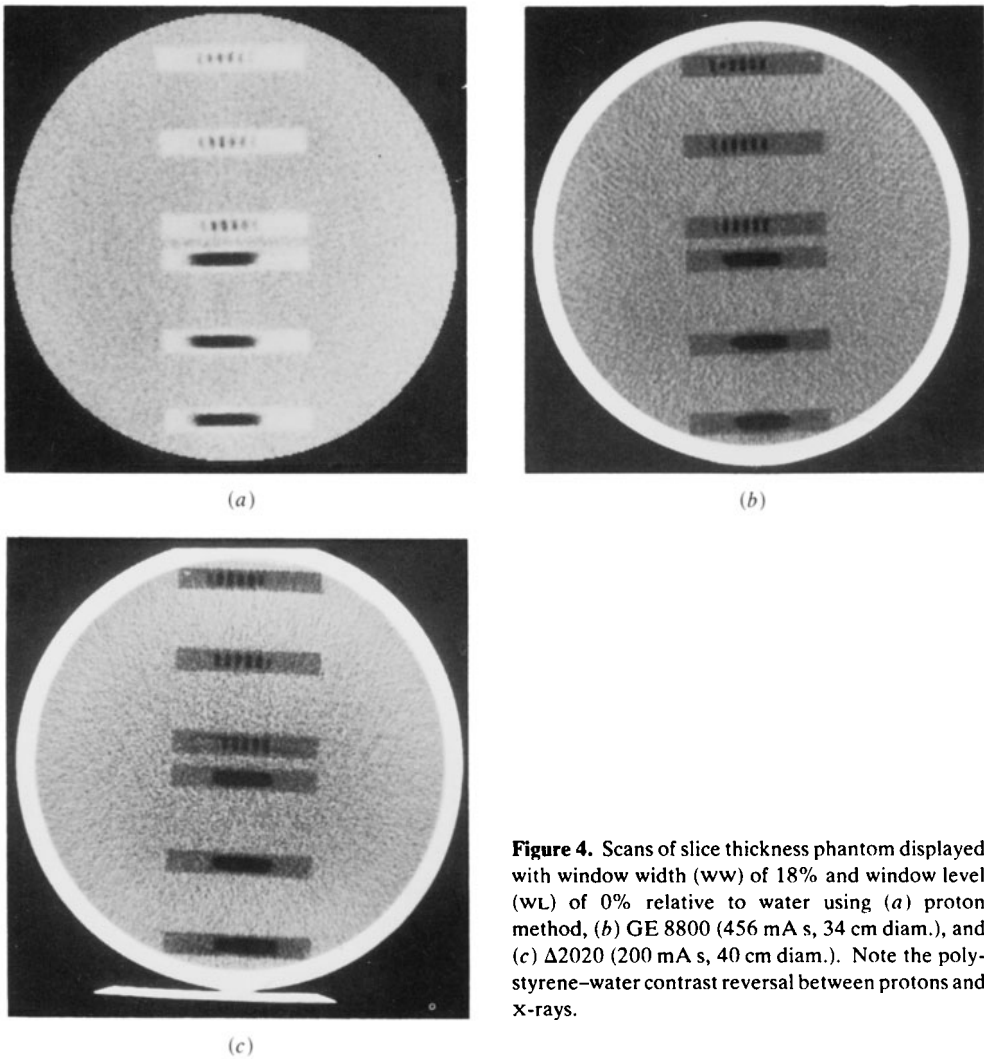
(a)

(b)

(c)

Figure 4. Scans of slice thickness phantom displayed with window width (WW) of 18% and window level (WL) of 0% relative to water using (a) proton method, (b) GE 8800 (456 mA s, 34 cm diam.), and (c) Δ2020 (200 mA s, 40 cm diam.). Note the polystyrene–water contrast reversal between protons and x-rays.

wide slot diagonally across a 6.4 mm thick sheet of polystyrene at the slope of 0.315. These were cemented between two 3.2 mm thick sheets to form a water-tight block. The ramps were positioned at distances of 1.0, 6.0, and 11.1 cm from the centre of the phantom. Three other blocks were constructed similarly except individual 2 mm diameter holes were drilled with 2 mm spacings in the slice thickness direction to provide a means of estimating slice thickness by visual inspection. For the x-ray scans, the phantom was placed in a Plexiglas cylinder, 27.9 cm in diameter, 1.3 cm thick wall, filled with water.

The slice thickness sensitivity profiles were obtained from the scans shown in figure 4 by plotting the CT reconstruction values of the ramps against position, suitably normalised to the longitudinal displacement. The results for the central ramp shown in figure 5 include blurring caused by the 2 mm wide slot. While the x-ray scanners have rather sharp sensitivity profiles, the proton profile is less well defined on account of multiple Coulomb scattering. The FWHM widths of the curves are 9.7 mm for the protons, 9.4 mm for the GE 8800, and 9.2 mm for the Δ2020. The sensitivity profiles
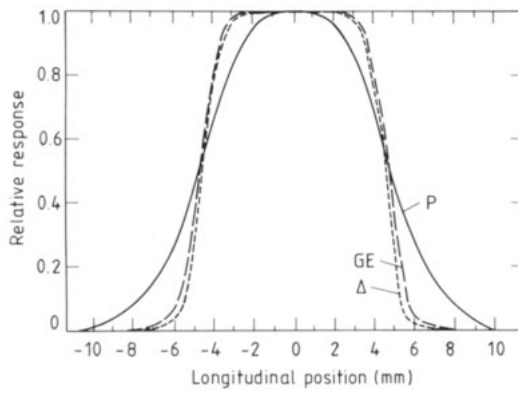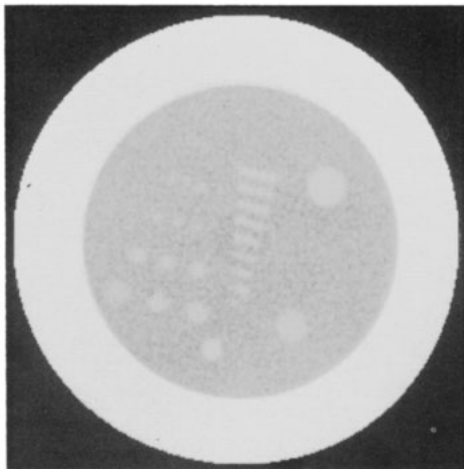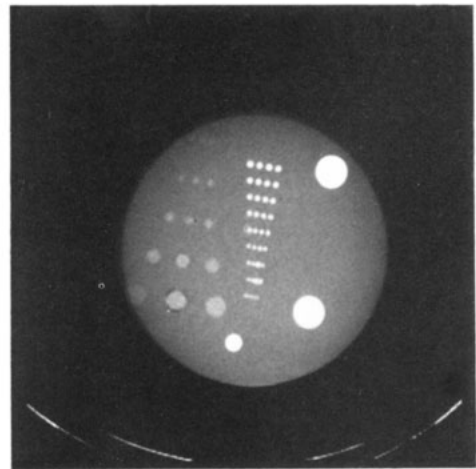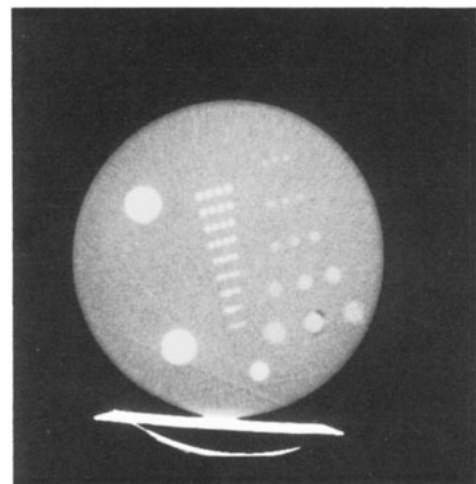
Figure 5. Central slice thickness sensitivity profiles derived from the scans shown in figure 4.

(a)

(b)

(c)

Figure 6. Polyethylene performance phantom (ww = 18%) scanned by (a) protons (wL = −2%), (b) GE 8800 (wL = −11%, 456 mA s, 34 cm diam.), and (c) Δ2020 (wL = −11%, 200 mA s, 25 cm diam.).

vary little with distance from the centre of the scan. The outermost ramp yielded widths of 10.1 mm, 8.7 mm, and 9.3 mm respectively. These widths are all reasonably close to the nominal slice thicknesses of 10 mm.

The relative average dose efficiencies of the scans shown in figure 4 are discussed in Appendix 1. The dose advantage of the proton method presented here is 4.0:1 compared to the GE 8800 and 21:1 compared to the Δ2020. Thus, the proton method retains its dose advantage even when compared to an x-ray scanner with very good dose efficiency such as the GE 8800.

Figure 6 shows scans of a 19.3 cm diameter polyethylene performance phantom used in earlier studies (Hanson *et al* 1981). Note that the window levels used in the proton and x-ray displays are different by 10% owing to the different response of these two techniques to polyethylene relative to water. The relative ability to detect the low contrast (1.8%) discs in these images is consistent with the estimated NEQ values, 1.27×10^7 mm^{-1} for the proton method, 12.6×10^7 mm^{-1} for the GE 8800, and 7.40×10^7 mm^{-1} for the Δ2020. In the x-ray scans the NEQs have increased dramatically over
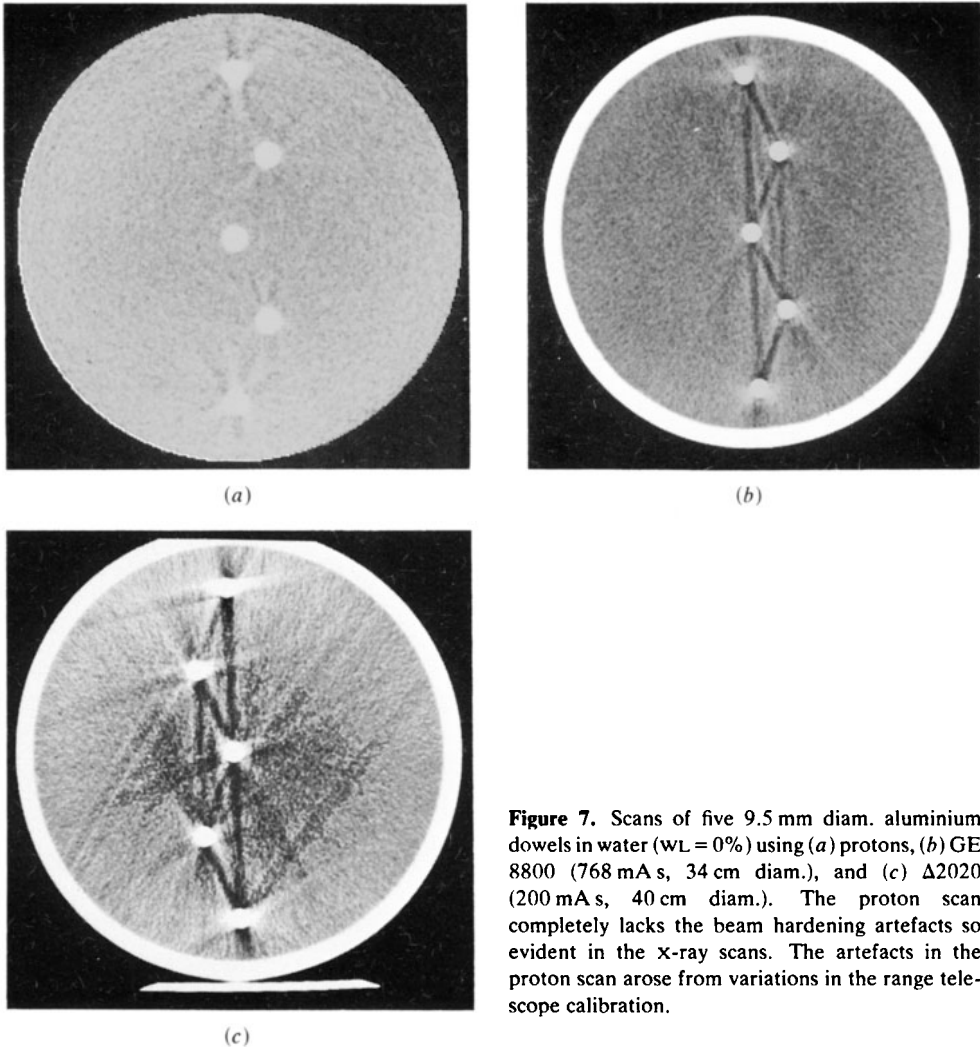
(a)

(b)

(c)

Figure 7. Scans of five 9.5 mm diam. aluminium dowels in water (WL = 0%) using (*a*) protons, (*b*) GE 8800 (768 mA s, 34 cm diam.), and (*c*) Δ2020 (200 mA s, 40 cm diam.). The proton scan completely lacks the beam hardening artefacts so evident in the x-ray scans. The artefacts in the proton scan arose from variations in the range telescope calibration.

those for figure 4 because of the much smaller diameter of the polyethylene phantom, 19.3 cm. The spatial resolution of the x-ray scans is clearly better than the proton scan. The width of the proton point spread function derived from the edge response to the nylon cylinder (upper left in figure 6(a) is 3.4 mm FWHM.

The results of scanning five aluminum rods of 9.5 mm diameter immersed in a water bath are shown in figure 7. The last two scans show typical beam hardening streak artefacts that are often difficult to remove from single-kV_p x-ray CT reconstructions, especially when more than two types of materials, e.g., muscle and bone, are present. Significantly, the proton reconstruction does not possess this type of artefact, making the proton technique particularly desirable for scanning inhomogeneous material. The artefacts in the proton scan, particularly visible in the outer rods, were produced by local variations in the range telescope calibration as a function of range that were not taken into account in the reconstruction process.

The scans of two human specimens are shown in figures 8 and 9. Figure 8 depicts the fixed heart specimen of a victim of a heart attack. The myocardial infarction, appearing
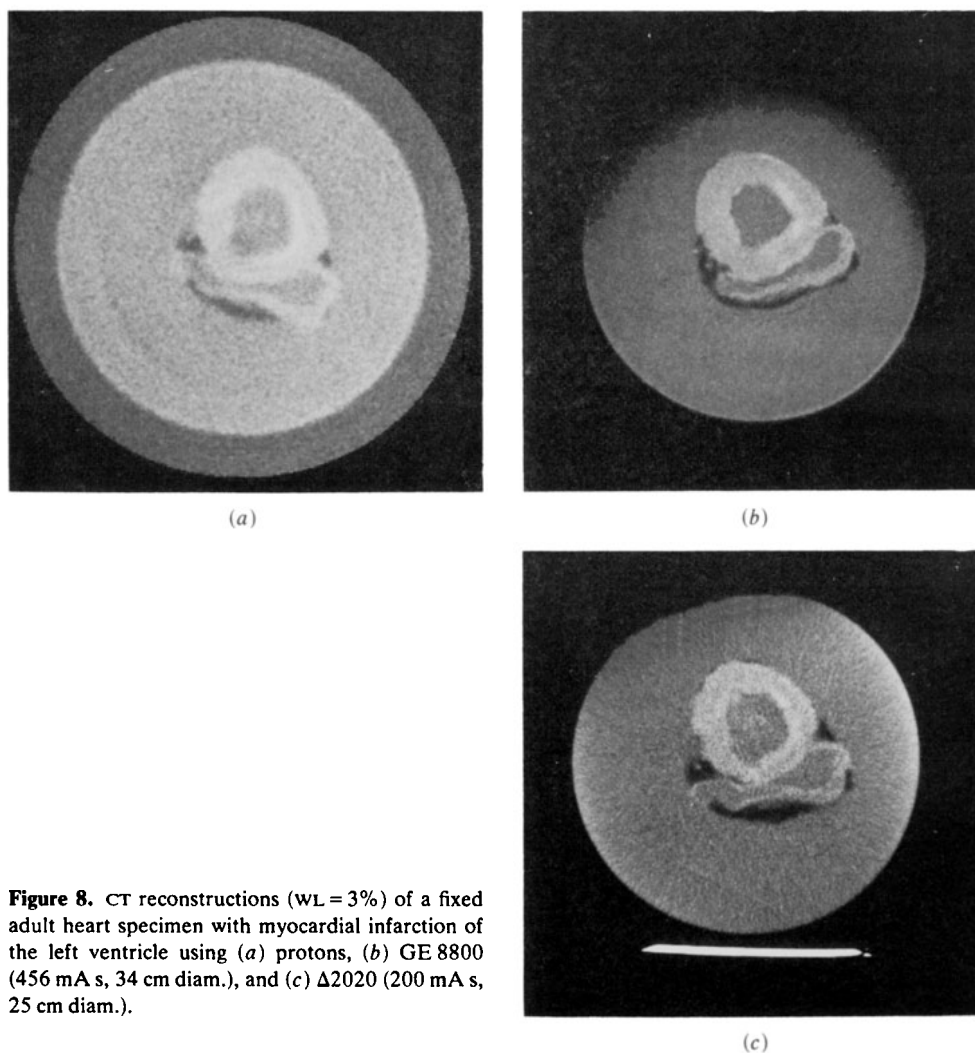

(a)

(b)

(c)

Figure 8. CT reconstructions (WL = 3%) of a fixed adult heart specimen with myocardial infarction of the left ventricle using (a) protons, (b) GE 8800 (456 mA s, 34 cm diam.), and (c) Δ2020 (200 mA s, 25 cm diam.).
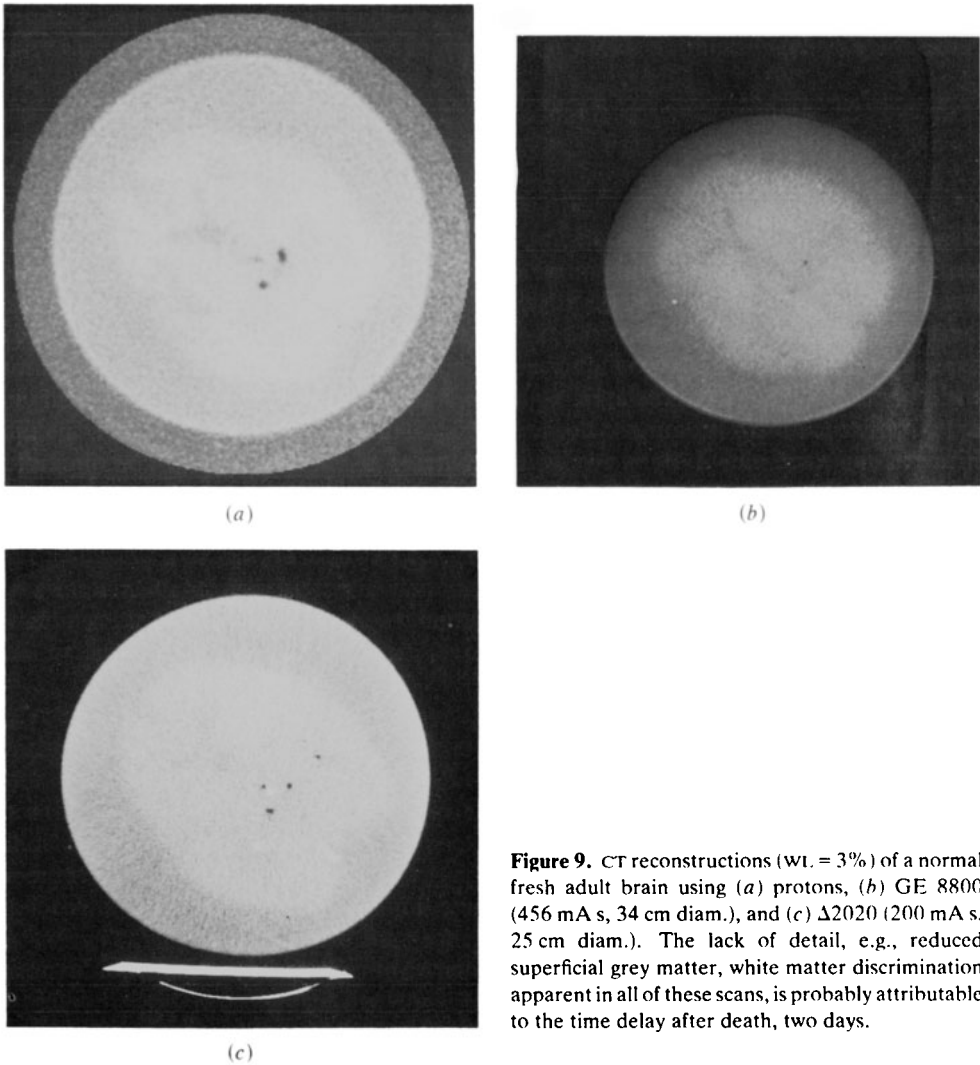
(a)

(b)

(c)

Figure 9. CT reconstructions (WL. = 3%) of a normal fresh adult brain using (a) protons, (b) GE 8800 (456 mA s, 34 cm diam.), and (c) Δ2020 (200 mA s, 25 cm diam.). The lack of detail, e.g., reduced superficial grey matter, white matter discrimination apparent in all of these scans, is probably attributable to the time delay after death, two days.

as a region of decreased lucency on the inner wall of the left ventricle, is equally well visualised on all three scans. A layer of fat surrounding the right venticle appears darker in the x-ray scans than in the proton scan because of the lower effective atomic number of fat. The difference in the appearance of the fat observed in the GE 8800 scan suggests that the longitudinal position of this can is slightly displaced from the other two as a result of a misalignment of the laser reference in that unit. This displacement can result in dissimilar images.

The brain scans of figure 9 do not show the usual differentiation of superficial grey matter from white matter as seen in living patients. A number of factors may contribute to this in the autopsy specimen such as rapid (within 4 h) increase in water concentration in the grey matter (Yates *et al* 1975). However, the basal ganglia and the gelatin-filled ventricles are observed. Furthermore, large dark areas are discernible in the centre of the rear lobes and on the sides of the frontal lobes in all scans. In addition to the scans presented here, we scanned numerous other specimens, including an intact thorax,

liver, spleen, and kidney. Overall, the proton technique has yielded results that are remarkably similar to the x-ray CT reconstructions.

5. Conclusions

We have found that the proton CT and x-ray CT methods produce remarkably similar images of human organ specimens. If the only advantage of the proton technique is better dose utilisation, the anticipated extra expense of implementing charged particle CT may not be justified for widespread routine diagnostic studies. However, this statement must be tempered by our observation of significant alteration in the imaging of the autopsy brain specimen from that expected in a normal brain study. Thus, further charged particle CT studies *in vivo* may demonstrate advantages not observed in these specimens. Charged particle CT may also be valuable for special purposes such as in treatment planning for charged particle therapy.

Appendix 1. Dose efficiency calculations

The scans shown in figure 4 were used to compare dose utilisation of the three scanning methods. The number of noise-equivalent quanta (NEQ) (Hanson 1979) detected in the x-ray projection measurements were determined in two ways. Both methods are based on NEQ values determined for the two x-ray scanners from noise spectrum measurements made on water bath scans (Hanson, in preparation). The diameters of the water bath phantoms were 30.6 cm for the GE 8800, and 35.5 cm for the Δ2020. The first method involved scaling the NEQ values by the mean square noise. The RMS noise in the water region was 0.61% for the GE scan and 0.96% for the Δ scan. In the second method the NEQ values were adjusted by $\exp(\mu \cdot \Delta D)$ where μ is the linear attenuation of water, taken as 0.19 cm^{-1}, and ΔD is the change in diameter. Both methods yielded essentially the same results: NEQ $= 1.73 \times 10^7$ mm^{-1} for the GE 8800 and 1.02×10^7 mm^{-1} for the Δ2020 with perhaps a 10% uncertainty. The NEQ for the proton scan was found by assuming that 100% change in reconstruction value relative to water is equivalent to a change of 0.19 cm^{-1} and by using the known relation between the RMS noise, 0.44%, and NEQ (Hanson 1979). Thus, NEQ $= 0.90 \times 10^7$ mm^{-1} for the proton scan. The NEQ values were checked by roughly computing the noise granularities in water regions of the reconstructions displayed in figure 4.

The doses for the x-ray scanners were determined from TLD measurements of the dose profiles on the same water phantoms described above. The Harshaw TLD-700 TLDs were cross-calibrated to doses delivered by a ^{60}Co source with an accuracy of better than 5%. The dose readings were multiplied by 0.86 to correct for the difference in response of these TLDs in the diagnostic energy region (50 to 100 keV) from that at

K M Hanson et al

^{60}Co energy (1.25 MeV)†. These dose profiles were integrated to obtain an average
surface dose for a series of scans with 10 mm step size. These were adjusted for
asymmetries in the surface dose distributions (Frey *et al* 1979). The average surface
doses were converted to average volume dose by multiplying the GE dose by 0.76 and
the Δ dose by 0.65 (Frey *et al* 1979). The final result in the average multiscan dose for
the GE 8800 was 2.1 cGy and for the Δ2020 was 6.5 cGy with a 15% accuracy.

The average proton dose is based on the energy lost in the phantom by the number
of incident protons required to obtain figure 4(*a*). The effective number of protons that
fell in the range histogram peaks was 31×10^6. The number of incident protons was
calculated by dividing this number by the following efficiencies: 0.68 for the fraction of
incident particles that made it through the water bath to the trigger counters; 0.80 for
the protons that hit the central nine horizontal wires of the MWPC, 0.80 for those that
were included in nine vertical wires, and 0.79 for the fraction of events falling in the
range peak. The average dose for a series of 10 mm wide slices was calculated to be
0.27 cGy, not including the loss of events arising from instrumental limitations. The
dose efficiency is proportional to the ratio of NEQ to average dose. The relative dose
efficiencies of the three scanning methods is 1 : 0.25 : 0.047 for the proton GE 8800 and
Δ2020 scans, respectively.

Résumé

Tomographie computérisée par protons d'échantillons humains.

Nous présentons le protocole expérimental et les résultats d'une étude comparative des caractéristiques
d'imagerie TC par protons et par rayons X. Nous discutons les images obtenues sur un cerveau et un coeur
humain. Les images produites par les protons sont similaires en ce qui concerne le contenu en informations
alors qu'elles onto un net avantage en ce qui concerne la dose.

Zusammenfassung

Protonen-Computertomographie am Menschen.

Die experimentellen Bedingungen und die Ergebnisse einer vergleichenden Studie der Bildcharakteristiken
von Protonen- und Röntgenstrahlen-CT-Scans werden präsentiert. Scans des menschlichen Gehirns und des
Herzens werden diskutiert. Man fand, daß die durch Protonen erzeugten bilder in ihrem Informationsgehalt
ähnlich den durch Röntgenstrahlen erzeugten Bildern sind, jedoch einen entschiedenen Dosisvorteil liefern.

References

Brown D 1979 *IEEE Trans. Nucl. Sci.* **NS-26** 4606–13
Frey G D, Wise J D and Ross P 1979 *Proc. SPIE* **173** 216–24
Hanson K M 1979 *Med. Phys.* **6** 441
Hanson K M, Bradbury J N, Cannon T M, Hutson R L, Laubacher D B, Macek R J, Paciotti M A and Taylor
    C A 1981 *Phys. Med. Biol.* **26**
Janni J F 1966 *US Air Force Weapons Laboratory Technical Report* No AFWL-TR 65-150
Machen D R 1979 *IEEE Trans. Nucl.* **NS-26** 4618–22
—— 1980 in *Proc. Real Time Data Handling and Process Control* (Amsterdam: North-Holland) p 83–37
Wittenberg J, Maturi R A, Ferrucci J T and Margolies M N 1977 *J. Comput. Tomogr.* **1** 95–101
Yates A J, Thelmo W and Pappins H M 1975 *Am. J. Pathol.* **79** 555–64

† The energy dependence was measured by L Johnson (H-1) of Los Alamos National Laboratory.